Advantages of Persistent Cohomology in Estimating Animal Location From Grid Cell Population Activity

Daisuke Kawahara
8361405631@edu.k.u-tokyo.ac.jp
Shigeyoshi Fujisawa
shigeyoshi.fujisawa@riken.jp
Department of Complexity Science and Engineering, University of Tokyo, Kashiwa, Chiba 277-8563, Japan, and Laboratory for Systems Neurophysiology, RIKEN Center for Brain Science, Wako, Saitama 351-0198, Japan

Many cognitive functions are represented as cell assemblies. In the case of spatial navigation, the population activity of place cells in the hippocampus and grid cells in the entorhinal cortex represents self-location in the environment. The brain cannot directly observe self-location information in the environment. Instead, it relies on sensory information and memory to estimate self-location. Therefore, estimating low-dimensional dynamics, such as the movement trajectory of an animal exploring its environment, from only the high-dimensional neural activity is important in deciphering the information represented in the brain. Most previous studies have estimated the low-dimensional dynamics (i.e., latent variables) behind neural activity by unsupervised learning with Bayesian population decoding using artificial neural networks or gaussian processes. Recently, persistent cohomology has been used to estimate latent variables from the phase information (i.e., circular coordinates) of manifolds created by neural activity. However, the advantages of persistent cohomology over Bayesian population decoding are not well understood. We compared persistent cohomology and Bayesian population decoding in estimating the animal location from simulated and actual grid cell population activity. We found that persistent cohomology can estimate the animal location with fewer neurons than Bayesian population decoding and robustly estimate the animal location from actual noisy data.

1 Introduction

In neuroscience, advances in measurement techniques have made it possible to simultaneously record more than 700 neurons in silicon probes (Jun et al., 2017; Steinmetz et al., 2019) and more than 16,000 neurons in a two-photon microscope (Ota et al., 2021). Behind the high-dimensional neural activity, low-dimensional dynamics are hidden (Pandarinath et al., 2018; Gardner et al., 2022). Low-dimensional dynamics contain important

information that is not directly observable from higher-dimensional neural activity, such as task variables, the self-position in the environment, and sensory stimulus variables, such as the angle of visual stimuli. Therefore, estimating low-dimensional dynamics from only high-dimensional neural population activity is an important issue in neuroscience.

When an animal moves on a two-dimensional plane, grid cells in the entorhinal cortex fire at multiple positions, creating a triangular lattice in the plane (Hafting et al., 2005). Thus, information about self-position in the environment is represented by the population activity of grid cells. In this study, we estimate the animal location in the environment from the grid cell population activity without using the actual animal location information.

In previous studies, Bayesian population decoding using gaussian processes or artificial neural networks has estimated low-dimensional dynamics from high-dimensional neural activity. For example, a gaussian process method estimated the rat's location in its environment, a low-dimensional dynamics, from about 30 place cells recorded from the rat's hippocampus (Wu et al., 2017). Artificial neural network–based methods estimated the angle of visual stimuli, a low-dimensional dynamics, from the activity of 63 neurons recorded from the macaque primary visual cortex, the rat's location on a one-dimensional linear line from the activity of 100 grid cells generated by the simulations (Gao et al., 2016), and the monkey's hand trajectory from the activity of about 200 neurons recorded from the monkey's motor cortex (Pandarinath et al., 2018).

Another approach to Bayesian population decoding is a method that applies topology called persistent cohomology (Zomorodian & Carlsson, 2005). We describe an overview of persistent (co)homology below. In persistent cohomology, the topological structure of the data is examined in an n-dimensional space in which high-dimensional (n-dimensional) neural activity data are distributed. We consider each data point as an n-dimensional ball (or sphere) and gradually increase the balls' radius (see Figure 1A). The graph in Figure 1B is called barcode. In the vertical axis, H^k is called the homology group. Geometrically, it captures the presence of n-dimensional holes or voids in the topological space. Mathematically, it is defined as $H^k = Z^k/B^k$, where Z^k is the group of k-dimensional cycles and B^k is the group of k-dimensional boundaries (see section 4). The horizontal axis of the graph represents the radius of the n-dimensional balls. The length of the green line in the barcode indicates how long the hole in the data structure persists as the radius of the n-dimensional balls is increased. As the radius of the n-dimensional balls of data points is gradually increased, all the data points overlap to form a one-dimensional hole H^1, indicated by the red circle (see Figure 1A). The radius of the n-dimensional balls at this point is the start of the green line indicated by the arrow of H^1 (see Figure 1B). As the radius of the n-dimensional balls is further increased in Figure 1A, there is a timing when the one-dimensional hole H^1 disappears, as shown by the last arrow, and at this time, the green line indicated by the arrow of H^1 is
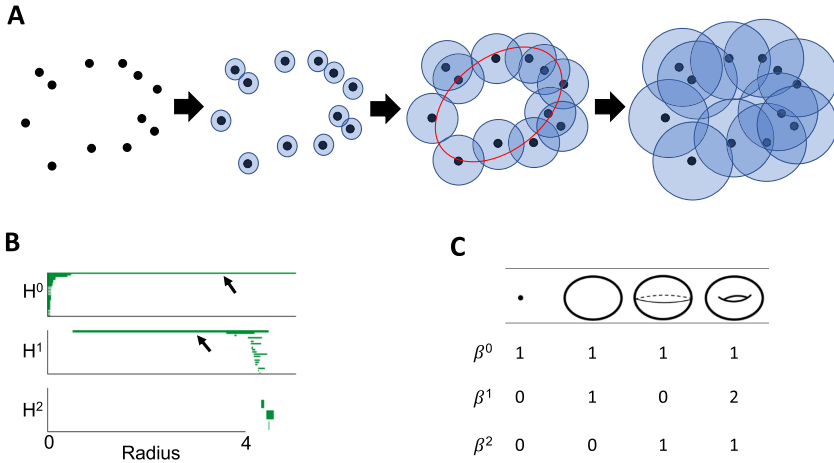
Figure 1. Schematic pictures of persistent cohomology. (A) Conceptual diagram of the change in data structure as the ball radius of the data points increases. Each data point corresponds to neural activity at each time point. (B) Barcode. H^n denotes the n-dimensional hole created by the set of data balls. As the radius of the data balls is increased, there is a time when the n-dimensional hole appears, which is the start time of the green line. The length of the green line corresponds to the duration of the n-dimensional hole as the radius of the data balls increases. (C) Example of topological classification of data structures based on the number of n-dimensional holes H^n. The numbers in the table are called Betti numbers (see section 4).

ended (see Figure 1B). The longer the barcode line, the more the hole reflects the topological features of the data structure. Short barcode lines are a weak topological feature of the data structure or reflect noise in the data. Depending on how many holes H^0, H^1, H^2 in each dimension have long barcode lines, we can find the topological data structure (see Figure 1C). The Betti number β^k is the rank of the homology group H^k and represents the number of k-dimensional holes in the topological space. For instance, β^0 represents the number of connected components, β^1 represents the number of loops, β^2 represents the number of voids, and so on. In Figure 1B, the long lines indicated by the arrows are $\beta^0 = 1, \beta^1 = 1, \beta^2 = 0$. Thus, we can find that the topological structure of the data is ring-shaped (see Figure 1C).

H^n contains the phase information (i.e., the value from 0 to 2π of each circular coordinate) of n-dimensional holes. We estimate the low-dimensional dynamics from the phase information of the manifold with n-dimensional holes formed by the high-dimensional neural activity data. However, persistent cohomology does not allow us to estimate low-dimensional dynamics from any high-dimensional neural activity. As shown in section 2,

persistent cohomology cannot estimate the animal location from the place cell population activity. The persistent cohomology method is valid only when low-dimensional dynamics are reflected on the manifold phase formed by high-dimensional neural population activity.

In previous studies, persistent cohomology has found a ring-shaped data structure $\beta^0 = 1$, $\beta^1 = 1$, $\beta^2 = 0$ in the population activity of place cells and head orientation cells (Dabaghian et al., 2012; Babichev et al., 2018; Akhtiamov et al., 2021; Rybakken et al., 2019; Chaudhuri et al., 2019). In particular, in the case of head direction cells, the animal head direction can be estimated from 0 to the 360-degree phase of the ring-shaped data structure. Also, persistent cohomology has revealed a two-dimensional torus structure $\beta^0 = 1$, $\beta^1 = 2$, $\beta^2 = 1$ in the activity of about 150 grid cells recorded from a rat exploring a two-dimensional plane (Gardner et al., 2022). It was also found that the animal location in 2D space is reflected in the phase of the 2D torus. Based on this fact, Kang et al. (2021) estimated animal location in the 2D plane by applying persistent cohomology to the simulated grid cell population activity.

Grid cells in rat and human brains are also found in 3D space (Grieves et al., 2021; Kim & Maguire, 2019). However, it is not known what the topological data structure is for the grid cell population activity while an animal moves through 3D space. In this study, we also address this issue through simulations. By applying persistent cohomology to the grid cell population activity generated by simulation, we found a 3D torus as a low-dimensional dynamics. Furthermore, we estimated the animal location in 3D space from the phase information of the three circular coordinates of the 3D torus.

While there are two methods for finding latent variables behind neural population activity, Bayesian population decoding, and persistent cohomology, it is unclear which is superior in estimating latent variables. We show that persistent cohomology can more accurately estimate the animal location (i.e., latent variables) from the simulated grid cell population activity in 2D and 3D space with fewer neurons than Bayesian population decoding. We also show that persistent cohomology can estimate the animal location more robustly than Bayesian population decoding for actual grid cell population activity.

2 Results

First, we compare persistent cohomology and Bayesian population decoding in estimating animal location in 2D space from the grid cell population activity. Next, we compare them in 3D space.

2.1 Estimation of Animal Location from Grid Cells in 2D Space. Figure 2A shows an example of the grid cell's receptive field, Figure 2B shows
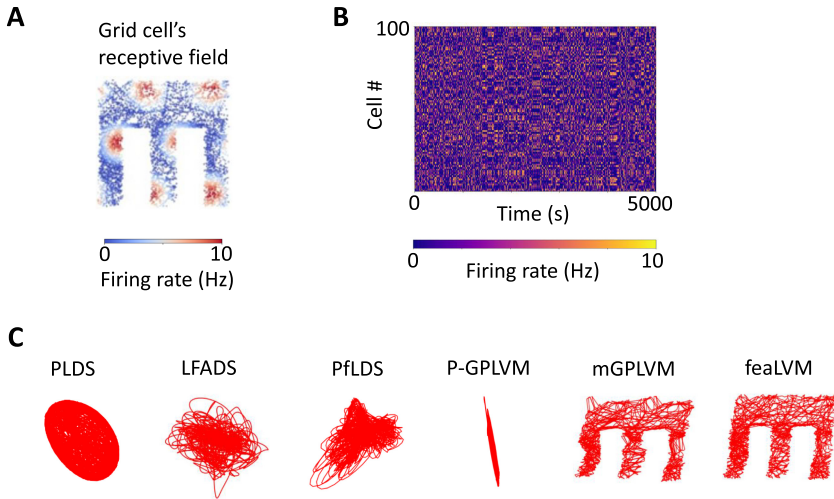
Figure 2. Estimation of animal location by Bayesian population decoding from simulated grid cells. (A) Receptive field of a grid cell. Other receptive fields of 100 grid cells are shown in Figure S2. (B) Raster plots of simulated 100 grid cells for 5000 seconds. (C) Estimation of animal location by previous methods. Here we show the best estimation results out of six experiments for each method. We changed the initial values of the model's parameters in each experiment. We set the random seeds to 42, 43, 44, 45, 46, and 47 in the six experiments. The hyperparameters of each model are the same as in the place cell experiment. See section 4.

the simulated population activity of 100 grid cells for 5000 seconds, and Figure 2C shows the estimation of animal location by the Bayesian population decoding methods.

PLDS (Macke et al., 2011), PfLDS (Gao et al., 2016), LFADS (Pandarinath et al., 2018), and P-GPLVM (Wu et al., 2017) use Euclidean space for latent variables and do not estimate well. On the other hand, mGPLVM (Jensen et al., 2020) and feaLVM (Bjerke et al., 2022) assume a 2D torus for the latent variables and can successfully estimate the animal location. The success is because the population activity space of grid cells is a torus (Gardner et al., 2022), and mGPLVM and feaLVM use the appropriate latent space.

Next, we used persistent cohomology to estimate the animal location in 2D space from grid cells in Figure 2B.

As shown by the arrows in Figure 3A, the long lines of the barcode indicating the features of the data structure are $\beta^0 = 1, \beta^1 = 2, \beta^2 = 1$, that is, a two-dimensional torus structure (see Figure 1C), which can be
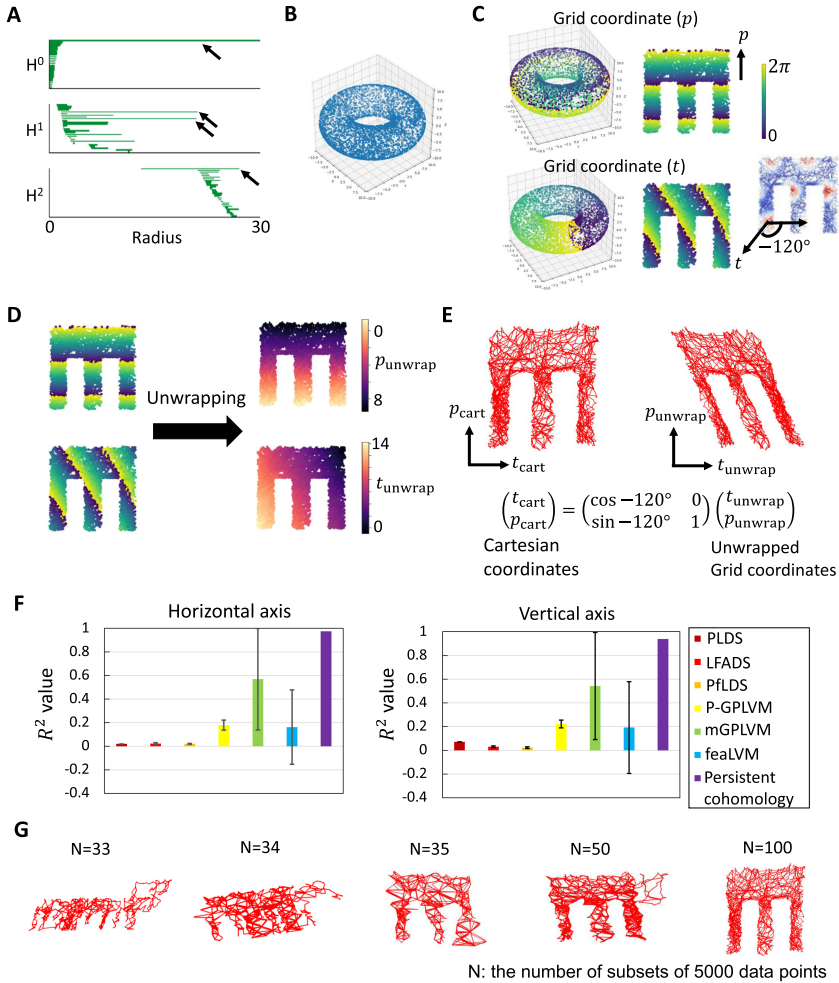
Figure 3. Estimation of animal location by persistent cohomology from simulated grid cells. (A) Barcode. (B) 2D torus structure. Each point corresponds to $\mathbb{R}^{100} \to \mathbb{R}^3$ neural activity at each time. (C) Torus phase 0 to 360 degrees and animal location at each time. (D) Unwrapping the torus circular coordinates. (E) Left: Estimated animal location after transformation to Cartesian coordinate or physical coordinate. (E) Right: Animal location estimated from the torus phase information. The circular coordinates t, p of the torus created by the activity of grid cells are not Cartesian in the physical world but oblique coordinates, as shown in panel C. Therefore, if t, p are set to Cartesian coordinates, the estimation results become oblique. (F) R^2 values with error bars. For the method using persistent cohomology, we show the result for $N = 100$ in sparse circular coordinates. (G) The result of sparse circular coordinates. N is the number of subsets of 5000 data points used to obtain the circular coordinates.

visualized in three-dimensional space using the estimated circular coordinates t, p ($0 \leq t \leq 2\pi, 0 \leq q \leq 2\pi$) by persistent cohomology as follows,

$$x = a \cos t + b \cos p \cos t,$$
$$y = a \sin t + b \cos p \sin t,$$
$$z = b \sin p, \tag{2.1}$$

where a, b are the radius of the large and small circles of the 2D torus $S^1 \times S^1$, respectively. Generally, the circular coordinates are calculated using persistent cohomology (Kang et al., 2021; Perea, 2018). Note that our letter's decoding by persistent cohomology also includes circular coordinates. (See section 4 for how to obtain the circular coordinates from persistent cohomology.) Figure 3B shows a 2D torus, the low-dimensional dynamics obtained from a high-dimensional ($n = 100$) grid cell activity. Each point in the torus corresponds to neural activity at each time point per second. The phase of the torus corresponds to the animal location and the scale of the grid pattern of the grid cell's receptive field (see Figure 3C).

Next, we considered estimating the animal location from the torus circular coordinates t, p. However, there are two problems with the estimation. The first is that the animal location is not uniquely determined due to the periodicity of the torus (see Figure 3C). Therefore, to eliminate the periodicity, we added 2π to the value of current circular coordinates for each round of the torus and subtracted 2π for each round of the torus in the opposite direction (see section 4.) Figure 3D shows the result of this unwrapping of the torus periodicity. The second problem is that the unwrapped circular coordinates t_{unwrap}, p_{unwrap} are not Cartesian coordinates. The direction in which the circulars coordinate t moves is tilted—120 degrees from the horizontal axis in our experiments (see Figure 3C). Therefore, if the unwrapped circular coordinates t_{unwrap}, p_{unwrap} are considered in the Cartesian coordinates directly, the estimated animal movement trajectory will be tilted (see Figure 3D, right). Therefore, we used a matrix to transform the unwrapped circular coordinates t_{unwrap}, p_{unwrap} into Cartesian coordinates t_{cart}, p_{cart} (see Figure 3E, bottom).

Moreover, we obtained the parameters of scaling a, translation b, and rotation θ to align the t_{cart}, p_{cart} with the animal trajectory coordinates x_{true}, y_{true} by minimizing the following equation,

$$\underset{a,b,\theta}{\arg\min} \left\| \begin{pmatrix} x_{true} \\ y_{true} \end{pmatrix} - a \begin{pmatrix} \cos\theta & -\sin\theta \\ \sin\theta & \cos\theta \end{pmatrix} \begin{pmatrix} t_{cart} \\ p_{cart} \end{pmatrix} + \begin{pmatrix} b_x \\ b_y \end{pmatrix} \right\|^2. \tag{2.2}$$

Through these operations, the persistent cohomology method could accurately estimate the animal location (see Figure 3F). Scaling and translation were performed for Bayesian population decoding as well. For mGPLVM

and feaLVM using toroidal latent space, the estimated circular coordinates were unwrapped and converted to Cartesian coordinates like for persistent cohomology.

Previous studies have used the explained deviance (Gardner et al., 2022) or the R^2 value (Wu et al., 2017) as a measure to evaluate the estimated latent variables. Explained deviance was computed to measure how well a Poisson generalized linear model (GLM) fitted to the spike count was at representing the data using either the toroidal coordinates or the tracked position as regressors (Gardner et al., 2022). However, since the objective of our study is to estimate the latent variable, animal location, we evaluated using the R^2 value, which directly compares the estimated latent variable to the animal location. Figure 3E shows the R^2 value calculated using the estimation results and the actual animal location. The R^2 value is defined as follows,

$$R^2 = 1 - \frac{\sum_i (s_i - \hat{s}_i)^2}{\sum_i (s_i - \bar{s})^2}, \tag{2.3}$$

where s_i is the animal location at time t_i, $\hat{s}_i$ is the estimated animal location at time t_i, and $\bar{s}$ is the average of the animal location. The closer R^2 is to 1, the closer the estimated value is to the actual animal location.

In addition, by using a technique called sparse circular coordinates (Kang et al., 2021; Perea, 2020; see section 4) in the persistent cohomology method, we could obtain circular coordinates from the subset of data points, $N = 100$ out of 5000 timepoints (see Figure 3G).

We then compared the estimation results of persistent cohomology and Bayesian population decoding using toroidal latent space (mGPLVM and feaLVM) for the number of simulated grid cells and timepoints. Persistent cohomology could accurately estimate the animal location from fewer neurons than Bayesian population decoding (see Figures 4A and 4B). When the total timepoints used for estimation were large, persistent cohomology was more accurate than Bayesian population decoding in estimating the animal location. However, when the total timepoints were small, Bayesian population decoding showed better estimation results (see Figures 4C and 4D).

Next, we examined the correspondence between the phase of the torus and the scale of the grid patterns of the receptive field of grid cells. The grid pattern's scale in the grid cell's receptive field decreases from ventral to dorsal in the entorhinal cortex (Hafting et al., 2005). We applied persistent cohomology to the simulated neural activity of 100 grid cells for each small and large grid pattern scale. We confirmed that the phase of the torus corresponds to the scale of the grid pattern of the receptive field (see Figure 5). The directions of circular coordinates p, t of the torus correspond to the orientations of the wavefronts of the grid patterns.

Finally, we estimated the rat's location from the neural activity of 149 grid cells recorded from the rat's entorhinal cortex during exploration on
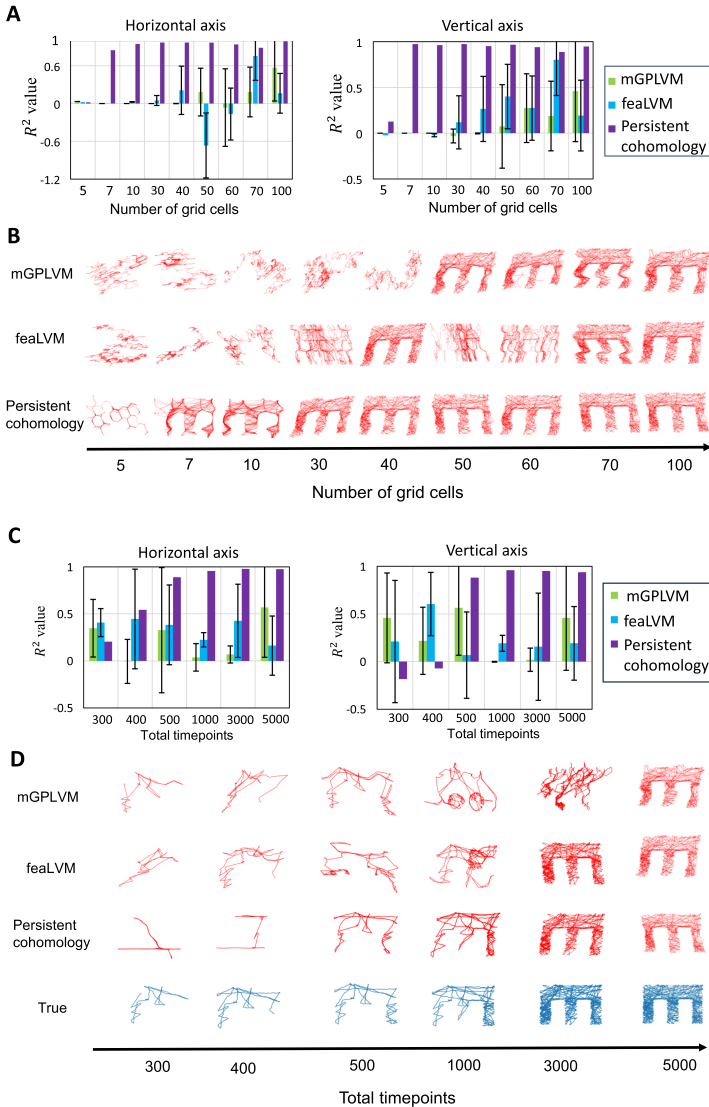
Figure 4. Comparison of persistent cohomology and Bayesian population decoding for number of simulated grid cells and timepoints. (A) R^2 values against the number of grid cells used for decoding. The N of sparse circular coordinates in persistent cohomology was set to 1000 for all numbers of neurons. (B) Estimated animal trajectory against the number of grid cells used for decoding. (C) R^2 values against the total timepoints used for decoding. For timepoints less than 1000, N of sparse circular coordinates in persistent cohomology was set to the same value as timepoints. N at 3000 timepoints was set to 1000. (D) Estimated animal trajectory against the total timepoints used for decoding.
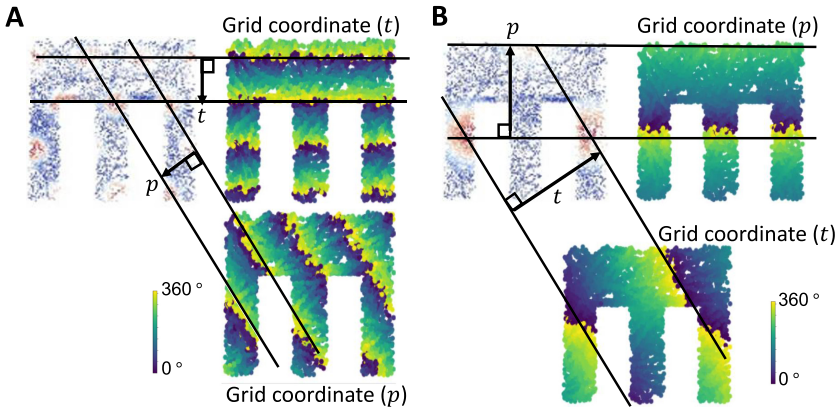
Figure 5. Correspondence between the circular coordinates p, t of a 2D torus and the simulated grid patterns. Regardless of the grid pattern scale, the directions of the circular coordinates t, p created by the grid cells' activity correspond to the directions of the wavefronts of the grid patterns indicated by the parallel lines. Other receptive fields of grid cells are shown in Figure S3. (A) Small grid scale. (B) Large grid scale.

the 2D plane (Gardner et al., 2022) (see Figure S5). We confirmed by persistent cohomology that the population activity of grid cells forms a 2D torus and that the torus phase reflects the rat's location (see Figure 6A). We estimated the rat's location from the torus phase using the same procedure as in the simulation (see Figure 6B). In sparse circular coordinates, we calculated the circular coordinates using a subset of $N = 1000$ out of 5000 total timepoints. The estimated result is smaller than the actual rat movement width in the y-axis (i.e., the vertical axis in the 2D plane). However, the timing of the vertical movement is almost identical. On the x-axis (i.e., the horizontal axis in the 2D plane), the estimated results almost coincide with the actual movement trajectory of the rat. One possible reason for the discrepancy in the y-axis is that the actual grid pattern of the rat's gird cell is slightly distorted than the grid pattern generated by the simulation (see Figure S5). For the actual grid cells data, persistent cohomology could estimate the animal location more accurately than Bayesian population decoding (see Figure 6C).

2.2 Estimation of Animal Location from Grid Cells in 3D Space. Experiments using fMRI indicate that the activity of grid cells in the entorhinal cortex when humans are exploring in 3D is a face-centered cubic lattice (Kim & Maguire, 2019). Therefore, we generated by simulation the activity in 20,000 s of 100 grid cells firing at the positions of a face-centered cubic (FCC) lattice. Figure 7A shows the raster plots of grid cells'
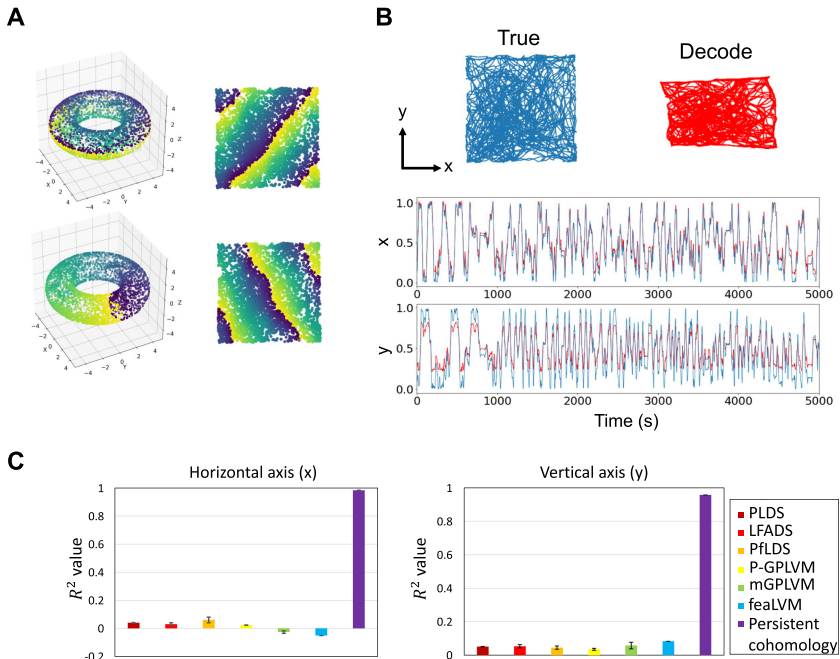
Figure 6. Estimation of rat's location from the neural activity of 149 grid cells recorded from the rat's entorhinal cortex. (A) Torus phase and animal location at each time point. (B) Comparison of actual rat's trajectory (blue) and estimated rat's trajectory (red). (C) R^2 values with error bars. The experimental conditions are the same as in the simulation experiments except for the input data.

activity. Figure 7B (top) shows the receptive field of a grid cell firing at the positions of an FCC lattice. After applying persistent cohomology to the grid cell population activity, we found $\beta^0 = 1$, $\beta^1 = 3$, $\beta^2 = 3$, $\beta^3 = 1$ (see Figure 7C). This is topologically equivalent to a three-dimensional torus (Matveev, 2004; Bombin & Martin-Delgado, 2007).

The circular coordinates of the 3D torus (i.e., grid coordinates in Figure 8) by persistent cohomology reflect the grid patterns of the receptive field (see Figure 8A). However, mGPLVM and feaLVM could not estimate the circular coordinates well, and the unwrapping did not work (see Figure 8B).

As in the 2D case, for each of the three circular coordinates t, p, q of the 3D torus, we performed a 360-degree addition operation for each round of the torus and a 360-degree subtraction operation for each round in the opposite direction (see Figure 8B). After this unwrapping, we estimated the animal location x_{est}, y_{est}, z_{est} in 3D space from the intersection of three planes with normal vectors for each of the unwrapped circular coordinates t_{unwrap}, p_{unwrap}, q_{unwrap} (see Figure 8C). Moreover, we obtained the
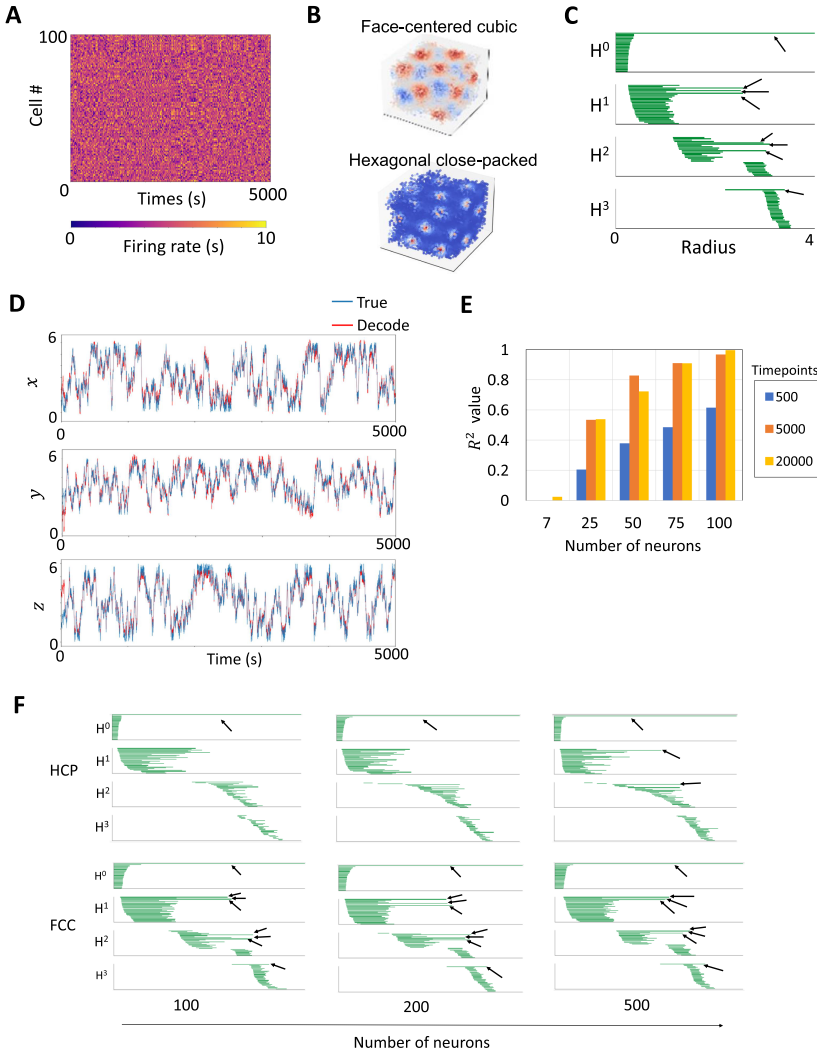
Figure 7. Estimation of animal location in 3D space by persistent cohomology from simulated grid cells. (A) Raster plots of simulated 100 grid cells for 5000 seconds. (B) Top: A receptive field of a grid cell firing at the positions of a face-centered cubic lattice. Bottom: A receptive field of a grid cell firing at the positions of a hexagonal closely packed lattice. The receptive fields of other grid cells are shown in Figure S6 (C) Barcode. $\beta^0 = 1$, $\beta^1 = 3$, $\beta^2 = 3$, $\beta^3 = 1$. (D) Comparison of actual animal location (blue) and estimated animal location (orange). $N = 1000$ in sparse circular coordinates. The number of grid cells = 100 and the timepoints = 20,000. (E) R^2 value at different timepoints and number of grid cells used for estimation. (F) Barcodes for population activity of grid cells firing at positions of hexagonal closely packed (HCP) and face-centered cubic (FCC).
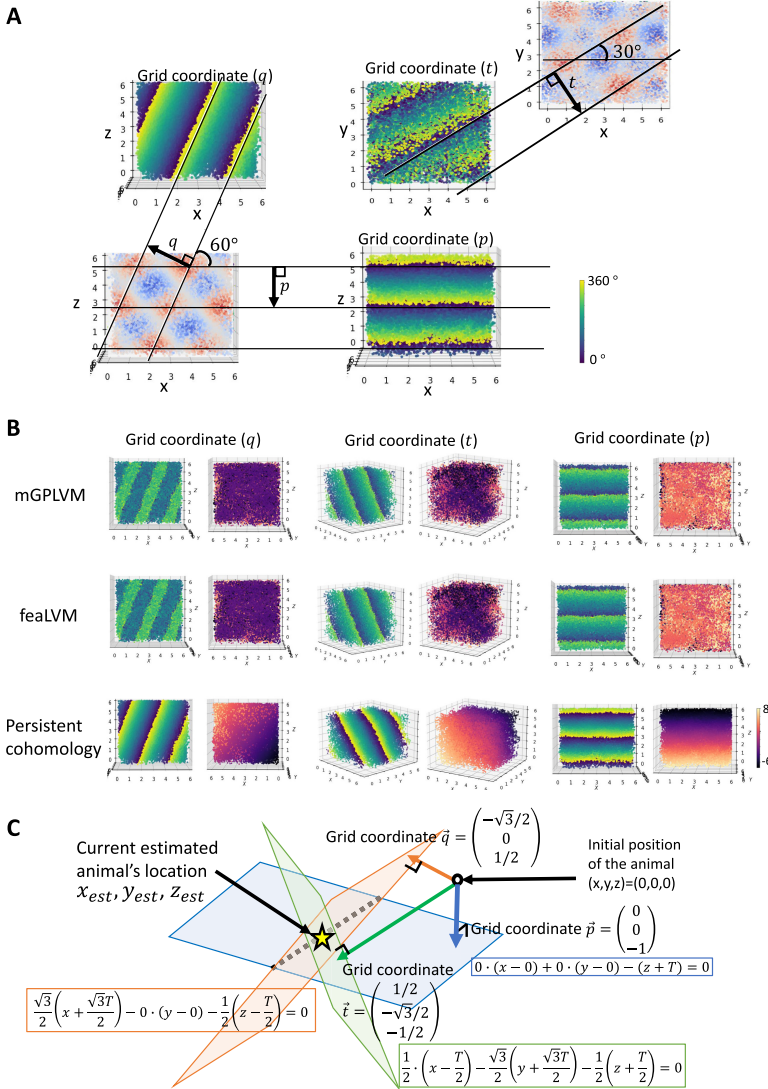
Figure 8. Correspondence between the circular coordinates (i.e., grid coordinates) p, q, t of the 3D torus and the simulated grid patterns. (A) As in 2D, the axis p, q, t of the 3D torus created by the grid cells' activity corresponds to the direction of the wavefront of the grid pattern indicated by the parallel lines. (B) Unwrapping the 3D torus circular coordinates. (C) Schematic diagram of the estimated animal location based on the intersection of the three planes with 3D-torus circular coordinates as normal vectors, respectively. The star represents the current estimated animal location, and the black dotted line represents the intersection of the two planes.

parameters of scaling a and translation b to align with the animal trajectory $x_{true}, y_{true}, z_{true}$ by minimizing the following equation:

$$\arg\min_{a,b} \left\| \begin{pmatrix} x_{true} \\ y_{true} \\ z_{true} \end{pmatrix} - a \begin{pmatrix} x_{est} \\ y_{est} \\ z_{est} \end{pmatrix} + \begin{pmatrix} b_x \\ b_y \\ b_z \end{pmatrix} \right\|^2. \tag{2.4}$$

Figure 7D shows the estimated animal location after the above scaling and translation. Figure 7E shows the R^2 value for the total timepoints used for decoding and the number of grid cells.

We also used persistent cohomology to analyze the population activity of grid cells firing at the hexagonal closely packed (HCP) positions shown in Figure 7B (bottom). However, we did not find a 3D torus like the FCC (see Figure 7F).

2.3 Applying Persistent Cohomology to the Place Cell Population Activity. Previous studies indicated that the manifolds formed by place cell population activity reflect the topological shape of the environment (i.e., global features of the environment) (Curto & Itskov, 2008; Curto, 2017). We applied persistent cohomology to the place cell population activity.

Figures 9A to 9D (upper left) show the movement trajectory of the animal for 10,000 seconds within four different forms of environment. The upper right of the panels shows the results of dimensional reduction of 100 place cell activities into 3D space by UMAP (McInnes et al., 2018). The manifold formed by the activity of place cells reflects the shape of the environment. From the barcode, we see that $\beta^0 = 1, \beta^1 = 0, \beta^2 = 0$ for the square and E-shape arenas; $\beta^0 = 1, \beta^1 = 1, \beta^2 = 0$ for the O-shape arena; and $\beta^0 = 1, \beta^1 = 2, \beta^2 = 0$ for the eight-shape arena (see Figure 9B). In the eight-shape arena, there are large and small holes, and this is to examine whether the hole size is reflected in the manifold created by the place cell population activity. In this experiment, there was little difference in the H^1 duration of the barcode reflecting the large and small holes. Therefore, we did not find detailed information about the shape of the environment in the manifold created by the place cell population activity. Figures 9C and 9D show the values of the circular coordinates at each time calculated using persistent cohomology, assigned to the animal location and the neural activity space by UMAP. The two circular coordinates estimated using persistent cohomology were able to characterize the two holes in the eight-shape arena with 0 to 2π, respectively.

Figure 9E shows that persistent cohomology could capture topological features of the environment with fewer neurons than Bayesian population decoding.
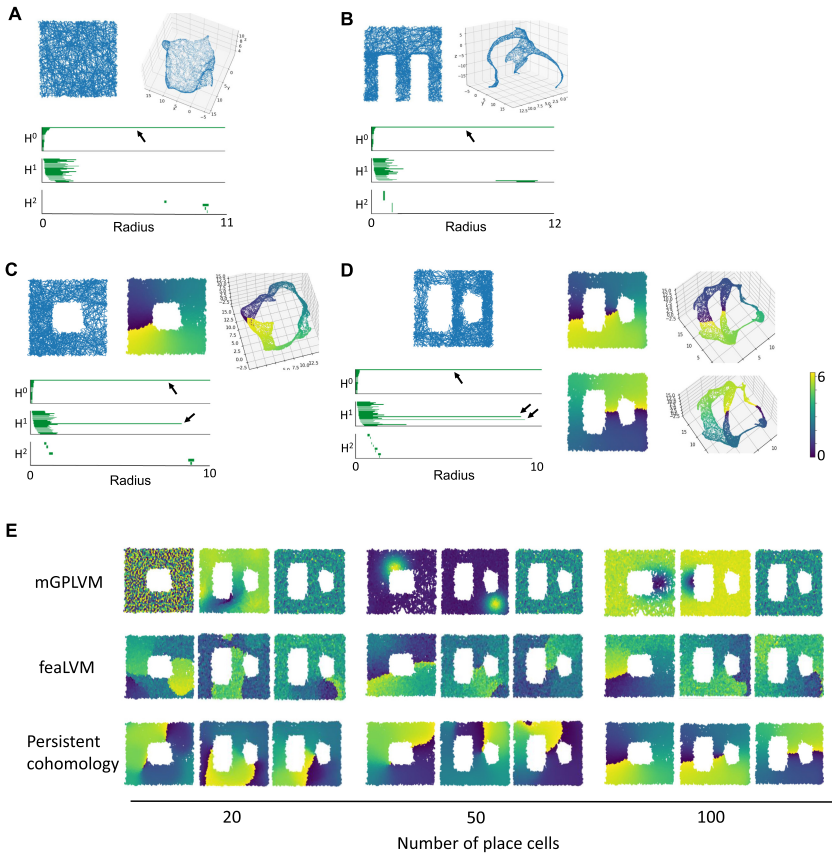
Figure 9. Persistent cohomology is applied to the simulated population activity of place cells. We can see that the topological shape of arena is reflected in the manifold created by place cells' activity. (A) Square-shape arena. (B) E-shape arena. (C) O-shape arena. (D) Eight-shape arena. For panels C and D we mapped the values of 0 to 2π at each time of the one-dimensional circular coordinate found by persistent cohomology from the population activity of 100 place cells to the animal location and to the neural activity space dimensionally visualized by UMAP. (E) Relationship between the circular coordinates estimated by mGPLVM, feaLVM, and persistent cohomolgy for different numbers of place cells and the animal location.

3 Discussion

The main contributions of this study follow:

- We have demonstrated the advantage of persistent cohomology over Bayesian population decoding in estimating the animal location from

the grid cell population activity. In the simulation, persistent coho-
mology could estimate the animal location in 2D with fewer neurons
than Bayesian population decoding (see Figure 4). For the actual grid
cell population activity, persistent cohomology could also estimate
the animal location more accurately than Bayesian population decod-
ing (see Figure 6).

- In the simulation, persistent cohomology found that the grid cell pop-
ulation activity on a face-centered cubic lattice of an animal moving
in 3D space results in a 3D torus structure (see Figure 8). Persistent
cohomology also estimated the circular coordinates of the 3D torus
more accurately than Bayesian population decoding and accurately
estimated the animal location in 3D space (see Figure 7D).

- Using persistent cohomology, we found that in 3D space, the grid
cell population activity firing at the location of the hexagonal closely
packed does not have clear circular coordinates like a 3D torus, mak-
ing it difficult to estimate the animal location (see Figure 7F).

- In the place cell population activity, we showed that persistent coho-
mology can estimate the environment's topology with fewer neurons
than Bayesian population decoding (see Figure 9).

In Figure 6C, persistent cohomology is more robust than Bayesian popu-
lation decoding in estimating animal location from the population activity
of real grid cells, including noise. It is possible that the animal location can
be estimated for other modules of real grid cells, as well as in simulation
results.

Although we were able to estimate the animal location from the activity
of grid cells using the persistent cohomology method, there are still some
problems.

The first issue is that, as shown in section 2, we could not estimate the an-
imal location from place cell activity using the persistent cohomology. The
previous method using gaussian processes has been able to estimate the an-
imal location from place cells' activity to some extent (see Figure S9). It may
be possible to determine the detailed shape of the environment by consid-
ering the dynamics of the short barcode lines as well as the long barcode
lines, a subject for future work.

The second issue is that we used the actual animal position information
to convert the coordinate system t, p of the phase of the 2D torus into a
Cartesian coordinate system. There are four possible angles between the
circular coordinates t, p: ± 120 degrees and ± 60 degrees. The transformation
matrix to the Cartesian coordinate system was obtained in this experiment
based on the animal location information. A possible approach that does
not use this information is to identify the direction of animal movement by
combining it with the activity of the head orientation cells (see Figures S7
and S8).

The third issue is that we could not understand the relationship between the direction of the wavefronts of grid pattern in 3D space and the direction of the circular coordinates t, p, q of the 3D torus. In the 2D space, there were four possible angles (± 120 and ± 60 degrees) between the circular coordinates t, p, which corresponded to the direction of wavefronts of the grid pattern. Investigating the possible angles between the circular coordinates t, p, q in the 3D space is work for the future.

The last issue is that while persistent cohomology could estimate the animal location more accurately than Bayesian population decoding for small numbers of neurons, persistent cohomology was inferior to Bayesian population decoding for small numbers of total timepoints. It is also future work to understand theoretically why persistent cohomology is better than Bayesian population decoding for small numbers of neurons and why Bayesian population decoding is better for small numbers of total timepoints.

In the previous study, the P-GPLVM can consistently attain R^2 values > 0.8 on simulated place cell data (Wu et al., 2017). Although the P-GPLVM in our experiment had $R^2 > 0.8$ on the horizontal axis (see Figure S9D), the R^2 value on the vertical axis is less than 0.8. This may be due to differences in the shape of the maze and the firing patterns of place cells used in the simulation. Also, the previous study with $R^2 > 0.3$ for grid cells was for animals moving on a one-dimensional track (Wu et al., 2017), while our experiment is two-dimensional and the R^2 value is smaller than 0.3 (see Figure 3F).

3.1 Applications of Persistent Cohomology. In addition to the representation of animal location, grid cells can also represent social relations (Park et al., 2021), the concept of things (Constantinescu et al., 2016), the visual sense (Staudigl et al., 2018; Killian et al., 2012) and smell (Bao et al., 2019), word meaning (Viganò et al., 2021), and mental simulation (Bellmund et al., 2016). This information represented by grid cells is expected to form the dynamics on the torus. Higher-order cognitive functions, such as the concept of objects, may be represented by a torus structure of three or more dimensions. Similar to the estimation of animal location, it would be possible to estimate the dynamics of cognition from the phase information of the higher-dimensional torus.

In addition, grid cells that represent location information are found not only in the entorhinal cortex but also in the secondary visual cortex (Long et al., 2021), somatosensory cortex (Long & Zhang, 2021), cingulate gyrus (Jacobs et al., 2013), hippocampal plateau (Boccara et al., 2010), and medial prefrontal cortex (Doeller et al., 2010). Persistent cohomology may help investigate how location information is shared and represented among brain regions.

4 Materials and Methods

The source code used in the experiment is available at https://drive
.google.com/drive/folders/1rDypHfXhtZURXNfZqiWSqahIZaC3Nuw8?
usp=sharing. We used Ripser for the persistent cohomology library (Tralie
et al., 2018).

4.1 Place Cells in 2D Space.
We generated the activity of the ith place
cell at animal position x, y as

$$f_i(x, y) = a \exp\left(-\frac{(x - \mu_{i_x})^2 + (y - \mu_{i_y})^2}{2\sigma^2}\right), \tag{4.1}$$

where $a = 40$ and $\sigma^2 = 15$ in the experiment. We randomly selected μ_{i_x}, μ_{i_y}
from a uniform distribution ranging from 0 to l. l is the arena's size, and in
this experiment, $l = 50$.

4.2 Grid Cells in 2D Space.
We used a continuous attractor neural net-
work model to generate the activity of grid cells by simulation (Guanella
et al., 2007). The activity of a neuron i at time $t + 1$, that is, $f_i(t + 1)$, is de-
fined as

$$f_j(t + 1) = (1 - \tau)B_j(t + 1) + \tau\left(\frac{B_j(t + 1)}{\sum_{i=1}^{N} f_i(t)}\right),$$

$$B_j(t + 1) = \sum_{i=1}^{N} f_i(t)w_{ij}(t),$$

$$w_{ij} = I \exp\left(-\frac{||\mathbf{c_i} - \mathbf{c_j}||^2}{\sigma^2}\right) - T, \tag{4.2}$$

where $\mathbf{c_i} = (c_{i_x}, c_{i_y})$ is the position of the cell i in 2D space. N is the number
of cells in the network. w_{ij} is the synaptic weight connecting neuron j to
neuron i, with $i, j \in \{1, 2, \dots, N\}$. I is the intensity parameter, defining the
strength of the synapses, σ regulates the size of the gaussian, and T is the
shift parameter. The parameter τ determines the stabilization strength.

4.3 Grid Cells in 3D Space.
The activity $f(\mathbf{r})$ of a grid cell firing at
a face-centered cubic lattice position $\mathbf{r}$ was calculated using the following
equations (Stella & Treves, 2015),

$$f(\mathbf{r}) = 1 + \frac{1}{4}\sum_{i=1}^{4}\cos(k_i \cdot \mathbf{r}), \tag{4.3}$$

$$k_i = \frac{2\pi}{a} \begin{pmatrix} 0 & 0 & \sqrt{3/2} \\ 2/\sqrt{3} & 0 & -1/\sqrt{6} \\ -1/\sqrt{3} & 1 & -1/\sqrt{6} \\ -1/\sqrt{3} & -1 & -1/\sqrt{6} \end{pmatrix}, \tag{4.4}$$

where a is the grid size, which was set to $a = 6$ in the experiment. The activity of the 3000 grid cells used in the experiment was generated by substituting $\mathbf{r} + \mathbf{\Delta r}$ into equation 4.3. $\mathbf{\Delta r}$ is a random number that follows a uniform distribution between $0 \sim 6$ on the x, y, and z axes.

4.4 Previous Methods. We explain the previous methods used in our experiments. See the source code (https://drive.google.com/drive/folders/1rDypHfXhtZURXNfZqiWSqahIZaC3Nuw8?usp=sharing) for the hyperparameters of the model used in the experiments.

4.4.1 Poisson Linear Dynamical System (Macke et al., 2011). The Poisson linear dynamical system (PTDS) is a generative model based on a linear dynamical system (LDS), which uses variational inference to estimate low-dimensional hidden dynamics $\mathbf{s}$ from neural activity $\mathbf{o}$. In LDS, low-dimensional hidden dynamics $\mathbf{s}$ evolves according to linear gaussian dynamics,

$$\mathbf{s}_{k,1} \sim \mathcal{N}(\mathbf{s}_0, Q_0),$$
$$\mathbf{s}_{k,t+1}|\mathbf{s}_{k,t} \sim \mathcal{N}(A\mathbf{s}_{k,t} + b_t, Q), \tag{4.5}$$

where k represents the number of trials in each experiment. In our experiment, we estimated the low-dimensional dynamics from a single trial $k = 1$. Conditioned on $\mathbf{s}$, the activity of neuron i at time t is given by a Poisson distribution,

$$o_{k,t,i}|\mathbf{s}_{k,t} \sim Poisson(\exp(C_i \mathbf{s}_{k,t,i} + d_i)), \tag{4.6}$$

where the matrix C determines how each neuron's activity is related to the hidden dynamics $\mathbf{s}_t$, and the vector d represents the mean firing rates of the population activity $\mathbf{o}$. PLDS uses an expectation-maximization (EM) algorithm to learn the parameters $\Theta = \{C, d, A, Q, Q_0, s_0\}$. The posterior distribution in the E-step is given by

$$\log P(\bar{\mathbf{s}}_k|\mathbf{o}_k, \Theta) = const + \sum_{t=1}^{T} \left(\mathbf{o}_{k,t}^T (C\mathbf{s}_{k,t} + d) - \sum_{i=1}^{q} \exp(C\mathbf{s}_{k,t,i} + d_i) \right)$$

$$- \frac{1}{2}(\mathbf{s}_{k,1} - \mathbf{s}_0)^T Q_0^{-1}(\mathbf{s}_{k,1} - \mathbf{s}_0)$$

$$- \frac{1}{2}\sum_{t=1}^{T-1}(\mathbf{s}_{k,t+1} - A\mathbf{s}_{k,t} - b_t)^T Q^{-1}(\mathbf{s}_{k,t+1} - A\mathbf{s}_{k,t} - b_t). \tag{4.7}$$

In the M-step, we update the parameters Θ by maximizing the following expected joint log-likelihood:

$$L(\Theta') = \sum_k \int [\log P(\mathbf{o}_k|\mathbf{s}, \Theta') + \log P(\mathbf{s}|\Theta')] \mathcal{N}(\mathbf{s}|\mu_k, \Sigma_k) d\mathbf{s}. \tag{4.8}$$

We used a global Laplace approximation (Yu et al., 2008) to get the mean μ_k and the covariance Σ_k.

4.4.2 PfLDS (Gao et al., 2016). PfLDS is a modification of PLDS, which models the relationship between low-dimensional dynamics $\mathbf{s}$ and neural activity $\mathbf{o}$ using artificial neural networks. In PfLDS, equation 4.6 is rewritten as

$$o_{k,t,i}|\mathbf{s}_{k,t} \sim Poisson(f_\psi(\mathbf{s}_{k,t,i})), \tag{4.9}$$

where f_ψ is an arbitrary continuous function from the hidden dynamics $\mathbf{s}_t$ into the spike rate. We represent $\mathbf{s}_t$ through a feedforward neural network model. In variational inference, we approximate the intractable posterior distribution $p_\theta(\mathbf{s} \mid \mathbf{o})$ by a tractable distribution $q_\phi(\mathbf{s} \mid \mathbf{o})$ and learn the model parameters $\theta = (\mu_1, Q_1, A, Q, \psi)$ by maximizing the evidence lower bound (ELBO) of the marginal log-likelihood:

$$\log p_\theta(\mathbf{o}) \geq \mathcal{L}(\theta, \phi; \mathbf{o}) = \sum_{k=1}^K \mathbb{E}_{q_\phi(\mathbf{s}_k|\mathbf{o}_r)} \left[\log \frac{p_\theta(\mathbf{o}_r, \mathbf{s}_k)}{q_\phi(\mathbf{s}_r|\mathbf{o}_k)} \right]. \tag{4.10}$$

4.4.3 Latent Dactor Analysis via Dynamical Systems (LFADS) (Pandarinath et al., 2018). In LFADS, the feedforward neural networks used in PfLDS are replaced by recurrent neural networks (RNNs). We estimate the low-dimensional dynamics $\mathbf{s}$ by minimizing the following loss function $\mathcal{L}^o - \mathcal{L}^{KL}$,

$$\log P(\mathbf{o}_{1:T}) \geq \mathcal{L}^o - \mathcal{L}^{KL}, \tag{4.11}$$

$$\mathcal{L}^o = \sum_{t=1}^T \log(Poisson(\mathbf{o}_t \mid \mathbf{r}_t))_{\mathbf{g}_0}, \tag{4.12}$$

$$\mathcal{L}^{KL} = D_{KL}(\mathcal{N}(\mathbf{g}_0 \mid \boldsymbol{\mu}^{g_0}, \boldsymbol{\sigma}^{g_0})||p^{g_0}(\mathbf{g}_0))_{\mathbf{g}_0}, \tag{4.13}$$

$$\mathbf{r}_t = \exp(W^{rate}\mathbf{s}_t),$$

$$\mathbf{s}_t = W^{latent}\mathbf{g}_t,$$

$$\mathbf{g}_t = \text{RNN}(\mathbf{g}_{t-1}, \mathbf{u}_t), \tag{4.14}$$

where matrices W^{rate} map low-dimensional dynamics $\mathbf{s}$ to neuron rates $\mathbf{r}$ and matrices W^{latent} maps $\mathbf{g}$ to $\mathbf{s}$. The priors for $\mathbf{g}_0$ and $\mathbf{u}_1$ are diagonal gaussian distributions. The prior for $\mathbf{u}_t$ with $t > 1$ is an autoregressive gaussian prior. See Pandarinath et al. (2018), for more details.

4.4.4 Poisson Gaussian-Process Latent Variable Model (P-GPLVM; Wu et al., 2017). In P-GPLVM, the latent variable dynamics $\mathbf{s}$ and the tuning curve f for the ith neuron are modeled by a gaussian process as follows:

$$\mathbf{s}_j \sim \mathcal{N}(\mathbf{0}, K_t), \tag{4.15}$$

$$\mathbf{f}_i \mid \mathbf{s}_{1:T} \sim \mathcal{N}(\mathbf{0}, K_x), \tag{4.16}$$

The spike count of the i'th neuron at t given the tuning curve f_i and latent variable dynamics $\mathbf{s}_t$ is Poisson distributed as

$$o_{i,t} \mid f_i, \mathbf{s}_t \sim Poisson(\exp(f_i(\mathbf{s}_t))). \tag{4.17}$$

We estimated the low-dimensional dynamics by the following maximum a posteriori (MAP) estimation,

$$\mathbf{s}_{\text{MAP}} = \arg \max_{\mathbf{s}} \sum_{i=1}^{N} q(\mathbf{o}_i \mid \mathbf{s}) p(\mathbf{s}), \tag{4.18}$$

$$\log q(\mathbf{o}_i \mid \mathbf{s}) = \log p(\mathbf{o}_i \mid \hat{\mathbf{f}}_i) - \frac{1}{2} \hat{\mathbf{f}}_i^T K_s^{-1} \hat{\mathbf{f}}_i - \frac{1}{2} \log |I_T + K_s W_i|, \tag{4.19}$$

where $W_i = -\nabla\nabla \log p(\mathbf{o}_i \mid \mathbf{f}_i), \hat{\mathbf{f}}_i = \arg \max_{\mathbf{f}} p(\mathbf{f}_i \mid \mathbf{o}_i, \mathbf{s})$, and I_T is the identity matrix (of size T).

4.5 Sparse Circular Coordinates. Sparse circular coordinates is a method for obtaining low-dimensional coordinates using only a subset of the data points $L \subset X$, called landmark points, in calculating persistent cohomology (Perea, 2020). We obtained the landmark points by maxmin sampling (De Silva & Carlsson, 2004). First, we randomly select $l_1 \in X$. Then, when $l_1, l_2, \cdots, l_{i-1}$ have chosen inductively, $l_i \in X \backslash \{l_1, l_2, \cdots, l_{i-1}\}$ is the data point that maximizes the function

$$x \mapsto \min\{D(x, l_1), D(x, l_2), \cdots, D(x, l_{i-1})\}, \tag{4.20}$$

where D is the metric space. Continue until the desired number of landmark points are selected. In Figure 3F, we set the number of landmark points to 33,34,35,50,100 for 5000 data points.
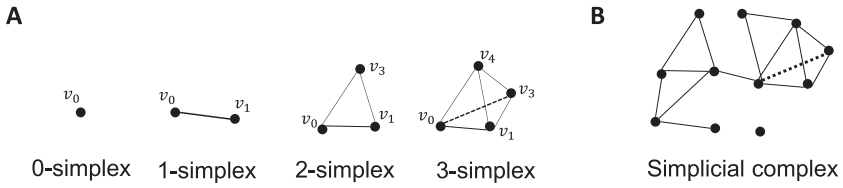
A

0-simplex   1-simplex   2-simplex   3-simplex   Simplicial complex

Figure 10. A simplicial complex is a set composed of n-simplex. (A) Example of n-simplex. From right to left: vertices, edges, triangles, and tetrahedron. (B) Example of a single complex.

4.6 Homology and Cohomology. Persistent cohomology creates barcodes for n-dimensional holes H^n created by high-dimensional neural activity data. We explain the homology and cohomology required to obtain H^n (Hatcher, 2002; Zomorodian & Carlsson, 2005).

A simplicial complex is a set consisting of n-simplex (see Figure 10).

The boundary of an n-simplex $\sigma = [V_0, V_1, \ldots, V_n]$ is composed of $n - 1$-simplex combinations. The boundary operator ∂_n is defined as

$$\partial_n \sigma = \partial[v_0, v_1, \ldots, v_n] = \sum_{i=0}^{n} (-1)^i [v_0, \ldots, \hat{v}_i, \ldots, v_n], \tag{4.21}$$

where $\hat{v}_i$ indicates that v_i is deleted from the sequence $[v_0, \ldots, v_n]$, that is, $\partial[v_0 v_1] = [v_1] - [v_0]$, $\partial[v_0 v_1 v_2] = [v_1 v_2] - [v_0 v_2] + [v_0 v_1]$, for example.

C_n, called n-chain groups, is an Abelian group with an n-simplex basis and is represented by the following equation with boundary operators:

$$\cdots \to C_n \xrightarrow{\partial_n} C_{n-1} \to \cdots \to C_1 \xrightarrow{\partial_1} C_0 \xrightarrow{\partial_0} 0. \tag{4.22}$$

For example, $\partial_1 : C_0 \to C_1$ is expressed as

$$
\partial_1 = \begin{array}{c} \\ [v_0] \\ [v_1] \\ [v_2] \end{array}
\begin{array}{ccc} [v_0 v_1] & [v_0 v_2] & [v_1 v_2] \end{array}
\left(\begin{array}{ccc} -1 & -1 & 0 \\ 1 & 0 & -1 \\ 0 & 1 & 1 \end{array} \right). \tag{4.23}
$$

The image (Im) of the boundary operators $B_n = \mathrm{Im}\,\partial_{n+1}$ is called the boundary group, and kernel (Ker) $Z_n = \mathrm{Ker}\,\partial_n$ is called the cycle group. Then the homology group $H_n = Z_n / B_n$ is defined.

When X^n is a set of n-simplex and R is a commutative ring, the element of $C^n = \{\text{function}\, f_n : X^n \to R\}$ is called the co-chain. The coboundary map d is expressed as

$$0 \xrightarrow{d_0} C^0 \xrightarrow{d_1} C^1 \to \cdots \to C^{n-1} \xrightarrow{d_n} C^n \to \cdots \tag{4.24}$$

When $Z^n = \mathrm{Ker}\, d_{n+1}$, the element of Z^n is called the cocycle, and when $B^n = \mathrm{Im}\, d_{n+1}$, the element of B^n is called the coboundary. Then the cohomology group $\mathrm{H}^n = Z^n/B^n$ is defined.

4.7 Persistent Cohomology. We used the Vietoris-Rips complex (VR) method to construct a single complex from a set of data points of higher-dimensional neural activity (Ghrist, 2008). Let $P = \{x_i \in \mathbb{R}^N \mid i = 1, \ldots, l\}$ be the set of l data points in N-dimensional space. In the VR complex, consider an N-dimensional sphere with radius r centered at each data point x_i in N-dimensional space. The following equation then defines the VR complex:

$$\mathrm{VR}(P) = \{\sigma \subseteq P \mid \forall x \neq y \in \sigma, \|x - y\| \leq r\}. \tag{4.25}$$

We obtain an increasing sequence of VR complexes $\mathrm{VR}(P, r_1) \to \cdots \to \mathrm{VR}(P, r_m)$ according to the increasing sequence $r_1 < \cdots < r_m$ of radius r, which is called filtration.

The $r_i(i = 1, \ldots, m)$ is the radius at which the simplex occurred. We obtain the sequence of cohomology for the increasing sequence of VR complexes as follows (Edelsbrunner et al., 2000; Zomorodian & Carlsson, 2005; Hatcher, 2002):

$$\mathrm{H}^n(\mathrm{VR}(P, r_1)) \leftarrow \mathrm{H}^n(\mathrm{VR}(P, r_2)) \leftarrow \cdots \leftarrow \mathrm{H}^n(\mathrm{VR}(P, r_m)). \tag{4.26}$$

In persistent cohomology, we can create the barcode by examining how long the element of $\mathrm{H}^n(\mathrm{VR}(P, r_i))$ persists for an increasing sequence of radius r. Those with long durations are considered significant topological features of the data structure, while those with short durations are considered noise. The Betti number is defined by $b_n = \dim \mathrm{H}^n$.

4.7.1 How to Obtain the Circular Coordinates of Torus. We describe a method for obtaining the circular coordinates of torus from high-dimensional neural activity data. (For more details, see De Silva et al., 2011 and Perea, 2018.) The n-dimensional torus T^n is represented as n direct products of the unit circumference S^1 as $T^n = S^1 \times S^1 \times \ldots S^1$. The next problem is to find the circular coordinates $\theta : X \to S^1$ that map from the VR complex X to S^1. We use the parameter f to define the circular coordinates θ on the VR complex X. Let the cocycle be $\alpha \in \mathrm{C}^1(X; \mathbb{R})$, and the smooth circular coordinates θ are obtained by minimizing the following equation:

$$\arg \min_{\bar{\alpha}} \left\{ \|\bar{\alpha}\|^2 \mid \exists f \in \mathrm{C}^1(X; \mathbb{R}), \bar{\alpha} = \alpha + d_0 f \right\}. \tag{4.27}$$

4.8 The Process of Unwrapping Periodicities in the Decoded Circular Coordinates. The latent space of population activity of grid cells in 2D and 3D space is a 2D and 3D torus, respectively. The circular coordinate of the

torus has a periodicity of 0 to 2π. In order to decode the animal location, it is necessary to unwrap this periodicity. In this experiment, when the animal moves per step, it rotates the circular coordinates on the torus by several tens of degrees at most. However, the values jump approximately 360 degrees only at the timing of one rotation of the torus. We unwrapped the periodicity by adding 2π to subsequent values of the circular coordinates when moving from 360 degrees to 0 degrees on the torus and subtracting 2π to subsequent values of the circular coordinates when moving from 0 degrees to 360 degrees.

Acknowledgments

References

Akhtiamov, D., Cohn, A. G., & Dabaghian, Y. (2021). Spatial representability of neuronal activity. *Scientific Reports*, *11*(1), 1–17. 10.1038/s41598-021-00281-y

Babichev, A., Morozov, D., & Dabaghian, Y. (2018). Robust spatial memory maps encoded by networks with transient connections. *PLOS Computational Biology*, *14*(9), e1006433. 10.1371/journal.pcbi.1006433

Bao, X., Gjorgieva, E., Shanahan, L. K., Howard, J. D., Kahnt, T., & Gottfried, J. A. (2019). Grid-like neural representations support olfactory navigation of a two-dimensional odor space. *Neuron*, *102*(5), 1066–1075. 10.1016/j.neuron.2019.03.034

Bellmund, J. L., Deuker, L., Schröder, T. N., & Doeller, C. F. (2016). Grid-cell representations in mental simulation. *eLife*, *5*, e17089. 10.7554/eLife.17089

Bjerke, M., Schott, L., Jensen, K. T., Battistin, C., Klindt, D. A., & Dunn, B. A. (2022). Understanding neural coding on latent manifolds by sharing features and dividing ensembles. In *Proceedings of the Eleventh International Conference on Learning Representations*.

Boccara, C. N., Sargolini, F., Thoresen, V. H., Solstad, T., Witter, M. P., Moser, E. I., & Moser, M.-B. (2010). Grid cells in pre- and parasubiculum. *Nature Neuroscience*, *13*(8), 987–994. 10.1038/nn.2602

Bombin, H., & Martin-Delgado, M. (2007). Exact topological quantum order in D = 3 and beyond: Branyons and Brane-Net condensates. *Physical Review B*, *75*(7), 075103. 10.1103/PhysRevB.75.075103

Chaudhuri, R., Gerçek, B., Pandey, B., Peyrache, A., & Fiete, I. (2019). The intrinsic attractor manifold and population dynamics of a canonical cognitive circuit across waking and sleep. *Nature Neuroscience*, *22*(9), 1512–1520. 10.1038/s41593-019-0460-x

Constantinescu, A. O., O'Reilly, J. X., & Behrens, T. E. (2016). Organizing conceptual knowledge in humans with a gridlike code. *Science*, *352*(6292), 1464–1468. 10.1126/science.aaf0941

Curto, C. (2017). What can topology tell us about the neural code? *Bulletin of the American Mathematical Society*, *54*(1), 63–78. 10.1090/bull/1554

Curto, C., & Itskov, V. (2008). Cell groups reveal structure of stimulus space. *PLOS Computational Biology*, *4*(10), e1000205. 10.1371/journal.pcbi.1000205

Dabaghian, Y., Mémoli, F., Frank, L., & Carlsson, G. (2012). A topological paradigm for hippocampal spatial map formation using persistent homology. *PLOS Computational Biology*, *8*(8), e1002581. 10.1371/journal.pcbi.1002581

De Silva, V., & Carlsson, G. E. (2004). Topological estimation using witness complexes. In *Proceedings of the First Eurographics Conference on Point-Based Graphic* (pp. 157–166).

De Silva, V., Morozov, D., & Vejdemo-Johansson, M. (2011). Persistent cohomology and circular coordinates. *Discrete and Computational Geometry*, *45*(4), 737–759. 10.1007/s00454-011-9344-x

Doeller, C. F., Barry, C., & Burgess, N. (2010). Evidence for grid cells in a human memory network. *Nature*, *463*(7281), 657–661. 10.1038/nature08704

Edelsbrunner, H., Letscher, D., & Zomorodian, A. (2000). Topological persistence and simplification. In *Proceedings of the 41st Annual Symposium on Foundations of Computer Science* (pp. 454–463).

Gao, Y., Archer, E. W., Paninski, L., & Cunningham, J. P. (2016). Linear dynamical neural population models through nonlinear embeddings. In D. Lee, M. Sugiyama, U. Luxburg, I. Guyon, & R. Garnett (Eds.), *Advances in neural information processing systems*, *29*. Curran.

Gardner, R. J., Hermansen, E., Pachitariu, M., Burak, Y., Baas, N. A., Dunn, B. A., . . . Moser, E. I. (2022). Toroidal topology of population activity in grid cells. *Nature*, *602*(7895), 123–128. 10.1038/s41586-021-04268-7

Ghrist, R. (2008). Barcodes: The persistent topology of data. *Bulletin of the American Mathematical Society*, *45*(1), 61–75. 10.1090/S0273-0979-07-01191-3

Grieves, R. M., Jedidi-Ayoub, S., Mishchanchuk, K., Liu, A., Renaudineau, S., Duvelle, É., & Jeffery, K. J. (2021). Irregular distribution of grid cell firing fields in rats exploring a 3D volumetric space. *Nature Neuroscience*, *24*(11), 1567–1573. 10.1038/s41593-021-00907-4

Guanella, A., Kiper, D., & Verschure, P. (2007). A model of grid cells based on a twisted torus topology. *International Journal of Neural Systems*, *17*(4), 231–240. 10.1142/S0129065707001093

Hafting, T., Fyhn, M., Molden, S., Moser, M.-B., & Moser, E. I. (2005). Microstructure of a spatial map in the entorhinal cortex. *Nature*, *436*(7052), 801–806. 10.1038/nature03721

Hatcher, A. (2002). *Algebraic topology*. Cambridge University Press.

Jacobs, J., Weidemann, C. T., Miller, J. F., Solway, A., Burke, J. F., Wei, X.-X., . . . Kahana, J. (2013). Direct recordings of grid-like neuronal activity in human spatial navigation. *Nature Neuroscience*, *16*(9), 1188–1190. 10.1038/nn.3466

Jensen, K., Kao, T.-C., Tripodi, M., & Hennequin, G. (2020). Manifold GPLVMs for discovering non-Euclidean latent structure in neural data. In H. Larochelle, M. Ranzato, R. Hadsell, M. F. Balcan, & H. Lin (Eds.), *Advances in neural information processing systems*, *33* (pp. 22580–22592), Curran.

Jun, J. J., Steinmetz, N. A., Siegle, J. H., Denman, D. J., Bauza, M., Barbarits, B., . . . Harris, T. D. (2017). Fully integrated silicon probes for high-density recording of neural activity. *Nature*, *551*(7679), 232–236. 10.1038/nature24636

Kang, L., Xu, B., & Morozov, D. (2021). Evaluating state space discovery by persistent cohomology in the spatial representation system. *Frontiers in Computational Neuroscience*, *15*, 28. 10.3389/fncom.2021.616748

Killian, N. J., Jutras, M. J., & Buffalo, E. A. (2012). A map of visual space in the primate entorhinal cortex. *Nature*, *491*(7426), 761–764. 10.1038/nature11587

Kim, M., & Maguire, E. A. (2019). Can we study 3D grid codes non-invasively in the human brain? Methodological considerations and FMRI findings. *NeuroImage*, *186*, 667–678. 10.1016/j.neuroimage.2018.11.041

Long, X., Deng, B., Cai, J., Chen, Z. S., & Zhang, S.-J. (2021). *A compact spatial map in V2 visual cortex.* bioRxiv.

Long, X., & Zhang, S.-J. (2021). A novel somatosensory spatial navigation system outside the hippocampal formation. *Cell Research*, *31*(6), 649–663. 10.1038/s41422-020-00448-8

Macke, J. H., Buesing, L., Cunningham, J. P., Yu, B. M., Shenoy, K. V., & Sahani, M. (2011). Empirical models of spiking in neural populations. In J. Shawe-Taylor, R. Zemel, Bartlett, F. Pereira, & K. Q. Weinberger (Eds.), *Advances in neural information processing systems*, *24*. Curran.

Matveev, V. S. (2004). Projectively equivalent metrics on the torus. *Differential Geometry and Its Applications*, *20*(3), 251–265. 10.1016/j.difgeo.2003.10.009

McInnes, L., Healy, J., & Melville, J. (2018). *UMAP: Uniform manifold approximation and projection for dimension reduction.* arXiv:1802.03426.

Ota, K., Oisi, Y., Suzuki, T., Ikeda, M., Ito, Y., Ito, T., . . . Murayama, M. (2021). Fast, cell-resolution, contiguous-wide two-photon imaging to reveal functional network architectures across multi-modal cortical areas. *Neuron*, *109*(11), 1810–1824. 10.1016/j.neuron.2021.03.032

Pandarinath, C., O'Shea, D. J., Collins, J., Jozefowicz, R., Stavisky, S. D., Kao, J. C., . . . Sussillo, D. (2018). Inferring single-trial neural population dynamics using sequential auto-encoders. *Nature Methods*, *15*(10), 805–815. 10.1038/s41592-018-0109-9

Park, S. A., Miller, D. S., & Boorman, E. D. (2021). Inferences on a multidimensional social hierarchy use a grid-like code. *Nature Neuroscience*, *24*(9), 1292–1301. 10.1038/s41593-021-00916-3

Perea, J. A. (2018). Multiscale projective coordinates via persistent cohomology of sparse filtrations. *Discrete and Computational Geometry*, *59*(1), 175–225. 10.1007/s00454-017-9927-2

Perea, J. A. (2020). Sparse circular coordinates via principal -bundles. In *Topological data analysis: The Abel Symposium 2018* (pp. 435–458). Springer.

Rybakken, E., Baas, N., & Dunn, B. (2019). Decoding of neural data using cohomological feature extraction. *Neural Computation*, *31*(1), 68–93. 10.1162/neco_a_01150

Staudigl, T., Leszczynski, M., Jacobs, J., Sheth, S. A., Schroeder, C. E., Jensen, O., & Doeller, C. F. (2018). Hexadirectional modulation of high-frequency electrophysiological activity in the human anterior medial temporal lobe maps visual space. *Current Biology*, *28*(20), 3325–3329. 10.1016/j.cub.2018.09.035

Steinmetz, N. A., Zatka-Haas, P., Carandini, M., & Harris, K. D. (2019). Distributed coding of choice, action and engagement across the mouse brain. *Nature*, *576*(7786), 266–273. 10.1038/s41586-019-1787-x

Stella, F., & Treves, A. (2015). The self-organization of grid cells in 3D. *eLife*, *4*, e05913. 10.7554/eLife.05913

Tralie, C., Saul, N., & Bar-On, R. (2018). Ripser.py: A lean persistent homology library for Python. *Journal of Open Source Software*, *3*(29), 925. 10.21105/joss.00925

Viganò, S., Rubino, V., Di Soccio, A., Buiatti, M., & Piazza, M. (2021). Grid-like and distance codes for representing word meaning in the human brain. *NeuroImage*, *232*, 117876.

Wu, A., Roy, N. A., Keeley, S., & Pillow, J. W. (2017). Gaussian process based nonlinear latent structure discovery in multivariate spike train data. In I. Guyon, Y. V. Luxburg, S. Bengio, H. Wallach, R. Fergus, S. Vishwanathan, & R. Garnett (Eds.), *Advances in neural information processing systems*, *30*. Curran.

Yu, B. M., Cunningham, J. P., Shenoy, K. V., & Sahani, M. (2008). Neural decoding of movements: From linear to nonlinear trajectory models. In *Neural Information Processing: 14th International Conference, ICONIP 2007* (pp. 586–595).

Zomorodian, A., & Carlsson, G. (2005). Computing persistent homology. *Discrete and Computational Geometry*, *33*(2), 249–274. 10.1007/s00454-004-1146-y

---